Hindawi
Advances in High Energy Physics
Volume 2020, Article ID 9386130, 8 pages
https://doi.org/10.1155/2020/9386130

Research Article

Elliptic Flow of Identified Particles in Pb–Pb Collisions at $\sqrt{s_{NN}} = 5.02$ TeV

Er-Qin Wang,[1] **Yin-Qun Ma**,[1] **Li-Na Gao**,[1] **and San-Hong Fan**[2]

[1]*Department of Physics, Taiyuan Normal University, Jinzhong, Shanxi 030619, China*
[2]*School of Life Science, Shanxi University, Taiyuan, Shanxi 030006, China*

Correspondence should be addressed to Er-Qin Wang; wangeq@tynu.edu.cn

Received 31 May 2019; Revised 23 July 2019; Accepted 5 August 2019; Published 27 January 2020

Academic Editor: Edward Sarkisyan-Grinbaum

In this paper, by using a Tsallis-Pareto-type function and the multisource thermal model, the elliptic flow coefficients of particles $\pi^{\pm}$, $K^{\pm}$, $p + \overline{p}$, $\Lambda + \overline{\Lambda}$, and K_S^0 produced in Pb–Pb collisions at the center-of-mass energy of $\sqrt{s_{NN}} = 5.02$ TeV are investigated. In the process of collisional evolution, because of geometric structure, pressure gradient, and thermal diffusion effects, deformation and translation occurred in the isotropic emission source, leading to anisotropy in the azimuth distribution of the final-state particles. Based on these dynamic factors, the dependence of elliptic flow on transverse momentum is described as well.

1. Introduction

As collision energy has gradually increased in recent years, high-energy physics has developed rapidly. On the one hand, the energy range of nucleus-nucleus collisions has been broadened [1–4]. On the other hand, the kinds of final-state particles measured by detectors have become more explicit [5–7]. This creates better conditions for obtaining a deep understanding of the collision mechanism. The distribution of high-energy final-state particles is important to understand the evolutionary mechanism of fluid dynamics, whereas the flow effect of final-state particles is meaningful for the new material form, quark-gluon plasma (QGP) [8–10]. The formation of QGP requires an extremely high-temperature, high-density environment. It is a state of released quarks and gluons that is similar to an ideal fluid. From an anisotropic azimuth analysis of final-state particles measured at the Relativistic Heavy Ion Collider (RHIC) [11] and the Large Hadron Collider (LHC) [12], it can be seen that the generated material unaffected by gravity is QGP under the condition of strong coupling. The quarks and gluons in the high-temperature, high-density state are affected by multiple factors. By means of the pressure gradient, the heterogeneity of energy density and the asymmetry of the geometric structure at the early stage of collisions are converted to the anisotropy of final-state particle momentum and finally manifest as the flow effect [13, 14].

In the evolutionary process of high-energy collisions, there are two main stages, chemical freeze-out and dynamic freeze-out. The former occurs in the formation stage of different kinds of particles, and the decay and generation of particles remain in dynamic balance. This is an inelastic collision process. The second process occurs later, in the diffusion stage. Momentum and energy are maintained in a thermal equilibrium state in an elastic collision process. After the two stages, as the temperature drops, the final-state particles are ejected from the action system. Various physical properties of the final-state particles are then measured by detectors, such as the longitudinal momentum spectrum [15, 16], the rapidity (pseudorapidity) distribution [17, 18], the multiplicity distribution [19, 20], and the flow effect [21–30]. By analysis of the final-state distribution using various theoretical models, the dynamic evolutionary mechanism, phase graph information, and particle attribution of quantum chromodynamics were deduced.

In noncentral nucleus-nucleus collisions, the main coefficient of the flow effect is the second-order harmonic, which is called elliptic flow (v_2). The value is used to represent collective motion in the system. Collective motion is one of the characteristics formed in collisions of QGP. The flow effect that is caused by the asymmetry of the initial geometric structure and the heterogeneous energy of the action system includes direct flow, elliptic flow, and triangular flow. All the

harmonics are quantified by the coefficient (v_n) of Fourier decomposition [31, 32]:

$$\frac{dN}{d\varphi} \propto 1 + 2\sum v_n \cos[n(\varphi - \Psi_n)]. \quad (1)$$

Similar long-range ridge structures and positive coefficients v_2 have been observed in experiments [21]. In theory, it is assumed that these are based on the collective effect caused by hydrodynamic evolution of colliding particles.

Previous studies [33–35] have presented a description of elliptic flow over a smaller range. Moreover, the isotropic hypothesis on the transverse plane and the translation and expansion effects of the emission source are used. In this paper, based on the multisource thermal model, using the distribution of the Tsallis-Pareto-type function, and at the center-of-mass energy of $\sqrt{s_{NN}} = 5.02$ TeV, the dependence of the elliptic flow of the identified particles ($\pi^{\pm}$, $K^{\pm}$, $p + \overline{p}$, $\Lambda + \overline{\Lambda}$, and K_S^0) in different centrality intervals in Pb–Pb collisions on transverse momentum is described [36]. The multisource thermal model is a statistical model that is based on the one-dimensional string model [37] and the fireball model [38] and was developed from the thermalized cylinder model [39, 40]. According to the multisource thermal model, many local emission sources are formed along the incident direction in high-energy collisions, and the final-state particles and jets are generated by these emission sources. In the rest frame of an emission source, the source is isotropic, that is, the final particles produced by the emission source are assumed to emit isotropically. Due to differences in impact parameters, centralities, position in space, or energy density, the emission source's temperature, excitation degree, and particle yield ratio may vary. In comparison with previous work [33–35] by the multisource thermal model, not only is the range of transverse momentum larger, but also the identification of the final-state particles is more accurate.

2. Model and Formulation

In this paper, using the multisource thermal model [41–45] and a Tsallis-Pareto-type function [46–49], the elliptic flow of identified particles in Pb–Pb collisions is analyzed. For each source in the multisource model, the Tsallis-Pareto-type function shows excellent reproducibility of the spectral measurement of many particles; the form is:

$$\frac{d^2N}{dyd p_T} = \frac{dN}{dy} K p_T \left[1 + \frac{m_T - m_0}{nC}\right]^{-n}, \quad (2)$$

where

$$K = \frac{(n-1)(n-2)}{nC[nC + (n-2)m_0]}, \quad (3)$$

$$m_T = \sqrt{m_0^2 + p_T^2}, \quad (4)$$

where m_0 is the rest mass, y is the rapidity, and N is the number of particles. According to some nonextensive thermodynamic particle models, the free parameter C, which is related to the average particle energy, represents the mean effective temperature in the interacting system, dN/dy is the particle output at different rapidity intervals, and n indicate the nonextensivity of the process, which is the departure of the spectra from the Boltzmann distribution. After integrating for rapidity, the distribution density function of the transverse momentum is:

$$f(p_T) = \frac{dN}{dp_T} = N_0 K p_T \left[1 + \frac{m_T - m_0}{nC}\right]^{-n}, \quad (5)$$

where N_0 denotes the normalization constant, which depends on the free parameters n and C. Hence, it is natural that $\int_0^\infty f(p_T)dp_T = 1$.

Related work [50] has shown that the transverse momentum distribution of the final-state particles formed in nucleus-nucleus collisions satisfies the Tsallis-Pareto-type function. In accordance with the Monte Carlo method, by Equation (5), the transverse momentum p_T can be extracted. In this expression, R_0 represents random numbers uniformly distributed on [0, 1], and p_T can be given as:

$$\int_0^{p_T} f(p_T)dp_T < R_0 < \int_0^{p_T + dp_T} f(p_T)dp_T. \quad (6)$$

Under the assumption of an isotropic emission source, the azimuth distribution of final-state particles is even, and the distribution function is:

$$f_\varphi(\varphi) = \frac{1}{2\pi}. \quad (7)$$

By the Monte Carlo method, the random number of the azimuth can be obtained as:

$$\varphi = 2\pi R, \quad (8)$$

where R represents a random number distributed on [0, 1]. Let the beam direction be the Oz axis, and let the reaction plane be the xOz plane. Therefore, the momentum components are

$$p_x = p_T \cos\varphi, \quad (9)$$

$$p_y = p_T \sin\varphi. \quad (10)$$

Due to the geometric structure of the participant, the pressure gradient, and interaction with the medium, the emission source deforms and translates in its rest frame. Hence, an anisotropic emission source is introduced in the multisource thermal model. To quantify the deformation and translation of the emission source, $a_x\,(a_y)$ and $b_x\,(b_y)$ express the deformation and translation of the emission source along the $Ox\,(Oy)$ axis, $a_x > 1$ (< 1) represents expansion (compression), and $b_x > 0$ (< 0) represents translation along the positive (negative) axis. Generally, for particles with different centrality intervals and transverse momentum, different $a_x\,(a_y)$ or $b_x\,(b_y)$ are obtained. As a first approximation, the empirical relationship can be expressed as:

$$a_x = 1 + k_1 \exp\left(-\frac{p_T}{\lambda_1}\right) + k_2 p_T, \quad (11)$$

where k_1, λ_1, k_2 are free parameters. For simplicity, the default is $a_y = 1$ and $b_{x,y} = 0$. Because of deformation, the above p_x is revised to become:

$$p'_x = a_x p_x + b_x. \tag{12}$$

Then the converted transverse momentum is:

$$p'_T = \sqrt{p'^2_x + p^2_y}. \tag{13}$$

Finally, the elliptic flow of final-state particles can be represented as:

$$v_2 = \left\langle \frac{p'^2_x - p^2_y}{p'^2_x + p^2_y} \right\rangle. \tag{14}$$

3. Comparisons with Experimental Data

Using the multisource thermal model, the anisotropic spectrum data of various particles generated in Pb–Pb collisions at $\sqrt{s_{NN}} = 5.02$ TeV [36] are studied and analyzed. The particles $\pi^{\pm}$, $K^{\pm}$, $p + \overline{p}$, $\Lambda + \overline{\Lambda}$, and K^0_S are located in different centrality intervals within 0–70% and depend on v_2 of the transverse momentum p_T. The rapidity is in the range $|y| < 0.5$. For particles $\pi^{\pm}$, $K^{\pm}$, and $p + \overline{p}$, the measurements in hypercenter collisions (0–1%) are also shown.

Figure 1 shows the elliptic flow $v_2(p_T)$ of meson $\pi^{\pm}$ generated in a Pb–Pb collision at energy $\sqrt{s_{NN}} = 5.02$ TeV in different centrality intervals. The data measured by the ALICE Collaboration in different centrality intervals are represented by different solid symbols, and the statistical and systematic errors are both considered in the error bar [36]. The curves are fitted to results generated by the Tsallis-Pareto-type function in the framework of the multisource thermal model. Table 1 shows the fitted free parameters (C, n, k_1, λ_1, and k_2), χ^2 and the degrees of freedom (dof). Clearly the model results are consistent with the experimental data. In the calculation, the data fitting indicates that the effective temperature C increases as the centrality percentage decreases, but that the value of n remains unchanged and is assumed to be 9. It is obvious that v_2 increases with p_T in the low p_T region, and then decreases slowly in the high p_T region. The transverse momentum corresponding to the maximum value increases with increasing particle mass. This trend is reflected in the values of k_1, λ_1, and k_2. Moreover, it is not hard to find that the parameter k_1 first increases rapidly with the centrality percentage and then slowly decreases. Finally, the values of χ^2/dof are in a reasonable range, which is not only affected by experimental errors, but is also related to the inaccuracy of the theoretical calculation results.

Figure 2 shows the $v_2(p_T)$ of $K^{\pm}$ in the given centrality interval. Similarly to Figure 1, the solid symbols also represent the experimental data recorded by the ALICE Collaboration, and the error bar includes the statistical and systematic errors. The curves are the results of fitting using the Tsallis-Pareto-type function. The fitting parameters χ^2 and dof are also listed in Table 1. It is apparent that the experimental data are well fitted by the model results. In the calculation, the values of effective temperature C decrease from the central to peripheral collisions and are systematically larger than those for particles

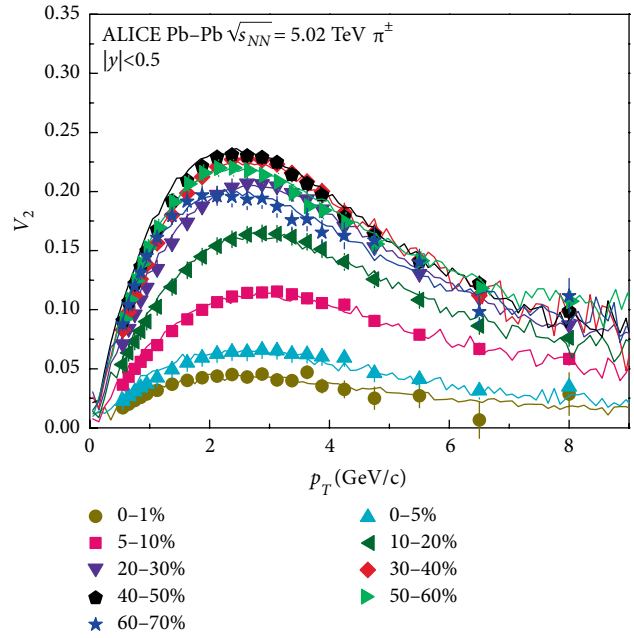

Figure 1: $v_2(p_T)$ of $\pi^{\pm}$ in a given centrality interval arranged into panels of various centrality classes [36]. The data, which were measured by the ALICE collaboration in various centrality classes, are represented in the figure by different symbols. Statistical and systematic uncertainties are shown as bars. The curves are the results of this study fitted using the Tsallis-Pareto-Type function and the multisource ideal gas model.

$\pi^{\pm}$. As the centrality percentage increases, the values of k_1 first increase rapidly, then slowly decrease, as shown in Figure 1.

Figure 3 shows the v_2 of $p + \overline{p}$, which depends on the transverse momentum. Figures 4 and 5 show the relationship between the elliptic flow and the transverse momentum spectrum of $\Lambda + \overline{\Lambda}$ and K^0_S, respectively. The solid symbols are the data points, and the curves show the model results. The fitted parameter values, dof and χ^2, are included in Table 1. It is evident that the fits are in good agreement with the experimental data. However, as shown in Figure 4, in the given centrality interval of 60–70%, there is a datum point located at $p_T = 9$ Gev/c that deviates seriously from the fitted value. The physical mechanism underlying this deviation is not yet understood. Similarly, when moving from central to peripheral collisions, C increases, and k_1 increases rapidly, then decreases slowly. Overall, the model fits the spectrum $v_2(p_T)$ of identified particles measured in different centrality intervals by ALICE in Pb + Pb collisions at approximately $\sqrt{s_{NN}} = 5.02$ TeV.

Based on the fitted results shown in Figures 1–5, Figure 6 shows the dependency relationship between the expansion factor a_x and the transverse momentum p_T in the given centrality interval for different particles $\pi^{\pm}$, $K^{\pm}$, $p + \overline{p}$, $\Lambda + \overline{\Lambda}$, and K^0_S. For a certain particle, $a_x(p_T)$ are different in different centrality intervals. The curves with maximum and minimum dependency relationship were chosen based on Equation (11) and are represented by solid and dashed lines, respectively. The variation trends are similar, but the ranges are slightly different. Furthermore, as the particle mass increases, the range also increases. Figure 7 shows the fitting parameter C,

Table 1: Values of C, n, k_1, λ_1, k_2, χ^2 number of degrees of freedom (dof) corresponding to the fits in Figures 1–5.

Figure	Particles	Centrality	C(GeV)	n	k_1	λ_1	k_2	χ^2/dof
Figure 1	$\pi^{\pm}$	0–1%	1.00	9	0.17	2.35	0.001	4/17
	$\pi^{\pm}$	0–5%	1.10	9	0.27	2.35	0.001	6/17
	$\pi^{\pm}$	5–10%	1.10	9	0.49	2.35	0.004	2/17
	$\pi^{\pm}$	10–20%	0.80	9	0.60	2.35	0.004	3/17
	$\pi^{\pm}$	20–30%	0.60	9	0.65	2.35	0.004	2/17
	$\pi^{\pm}$	30–40%	0.50	9	0.64	2.35	0.004	2/17
	$\pi^{\pm}$	40–50%	0.40	9	0.59	2.35	0.004	7/17
	$\pi^{\pm}$	50–60%	0.40	9	0.54	2.35	0.006	1/17
	$\pi^{\pm}$	60–70%	0.40	9	0.48	2.40	0.005	11/17
Figure 2	$K^{\pm}$	0–1%	2.60	9	0.28	2.35	0.000	5/12
	$K^{\pm}$	0–5%	2.20	9	0.40	2.35	0.000	12/12
	$K^{\pm}$	5–10%	1.70	9	0.66	2.35	0.002	8/12
	$K^{\pm}$	10–20%	1.25	9	0.86	2.25	0.002	4/12
	$K^{\pm}$	20–30%	1.00	9	0.98	2.15	0.003	2/12
	$K^{\pm}$	30–40%	0.72	9	0.83	2.35	0.002	6/12
	$K^{\pm}$	40–50%	0.68	9	0.84	2.20	0.002	2/12
	$K^{\pm}$	50–60%	0.55	9	0.64	2.35	0.003	1/12
	$K^{\pm}$	60–70%	0.40	9	0.44	2.40	0.005	1/12
Figure 3	$p+\overline{p}$	0–1%	3.50	9	0.40	2.40	0.002	10/15
	$p+\overline{p}$	0–5%	4.40	9	0.70	2.40	0.002	33/15
	$p+\overline{p}$	5–10%	2.80	9	1.05	2.35	0.002	25/15
	$p+\overline{p}$	10–20%	1.70	9	1.25	2.35	0.006	18/15
	$p+\overline{p}$	20–30%	1.30	9	1.25	2.35	0.007	23/15
	$p+\overline{p}$	30–40%	1.10	9	1.25	2.35	0.007	12/15
	$p+\overline{p}$	40–50%	0.95	9	1.10	2.35	0.006	8/15
	$p+\overline{p}$	50–60%	0.75	9	0.97	2.35	0.006	2/15
	$p+\overline{p}$	60–70%	0.75	9	0.77	2.35	0.006	1/15
Figure 4	$\Lambda+\overline{\Lambda}$	0–5%	4.20	9	0.58	3.00	0.005	12/7
	$\Lambda+\overline{\Lambda}$	5–10%	3.00	9	1.20	2.55	0.007	3/7
	$\Lambda+\overline{\Lambda}$	10–20%	2.10	9	1.57	2.30	0.009	2/7
	$\Lambda+\overline{\Lambda}$	20–30%	1.40	9	1.60	2.30	0.009	1/7
	$\Lambda+\overline{\Lambda}$	30–40%	1.10	9	1.42	2.40	0.009	1/7
	$\Lambda+\overline{\Lambda}$	40–50%	0.90	9	1.26	2.55	0.005	1/7
	$\Lambda+\overline{\Lambda}$	50–60%	0.80	9	1.07	2.50	0.009	1/7
	$\Lambda+\overline{\Lambda}$	60–70%	0.60	9	0.70	2.50	0.005	4/7
Figure 5	K_s^0	0–5%	2.10	9	0.38	2.20	0.002	3/8
	K_s^0	5–10%	1.70	9	0.65	2.20	0.002	2/8
	K_s^0	10–20%	1.20	9	0.78	2.20	0.006	1/8
	K_s^0	20–30%	0.90	9	0.83	2.20	0.005	1/8
	K_s^0	30–40%	0.70	9	0.79	2.20	0.008	1/8
	K_s^0	40–50%	0.60	9	0.73	2.20	0.006	1/8
	K_s^0	50–60%	0.55	9	0.63	2.40	0.003	1/8
	K_s^0	60–70%	0.40	9	0.44	2.45	0.005	1/8

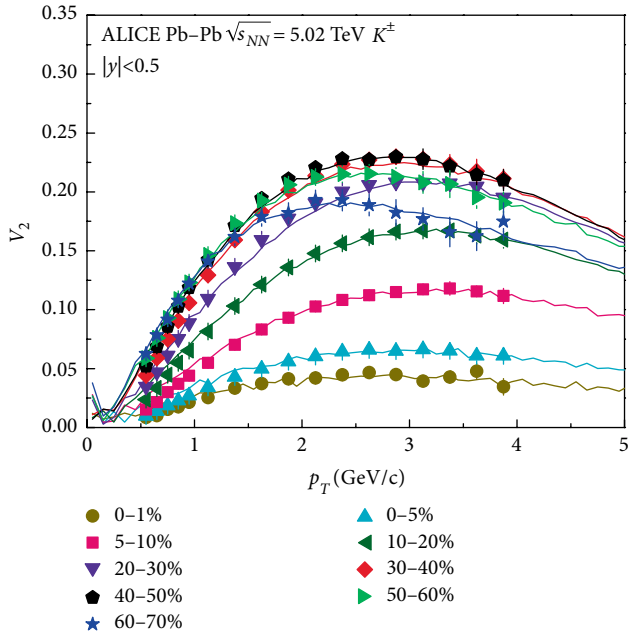

Figure 2: As for Figure 1, but showing $v_2(p_T)$ of $K^{\pm}$ for a given centrality [36].

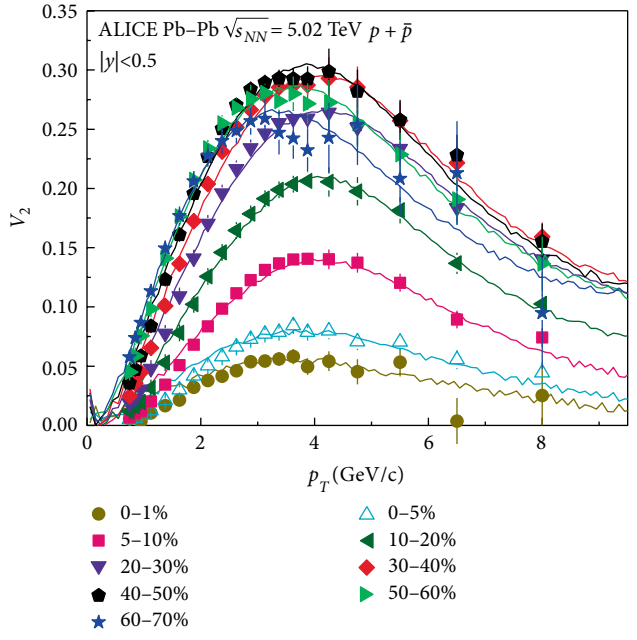

Figure 3: As for Figure 1, but showing $v_2(p_T)$ of $p + \bar{p}$ for a given centrality [36].

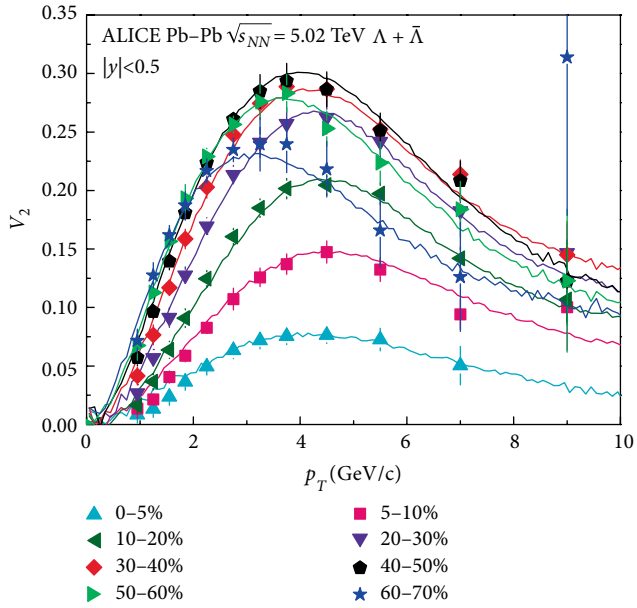

Figure 4: As for Figure 1, but showing $v_2(p_T)$ of $\Lambda + \bar{\Lambda}$ for a given centrality [36].

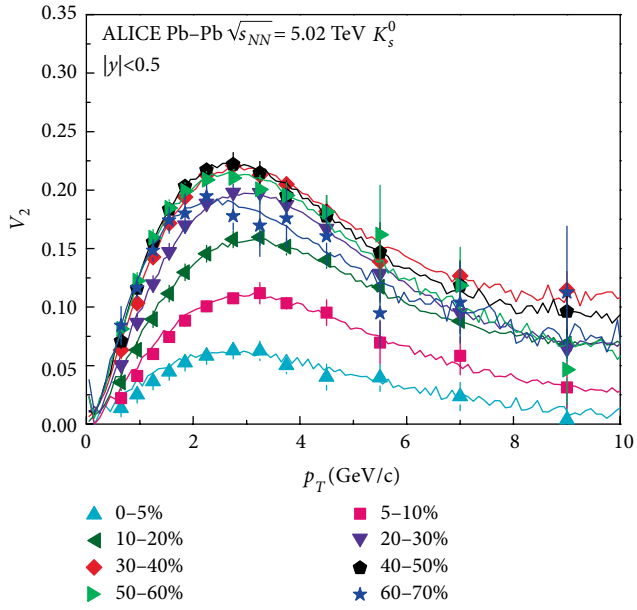

Figure 5: As for Figure 1, but showing $v_2(p_T)$ of K^0_s for a given centrality [36].

which depends on the variation of centrality. When moving from central to peripheral collisions, the effective temperature C gradually declines.

4. Discussion and Conclusions

According to the fitted results from the above comparisons, the fitted free parameter C is actually not the real temperature (the kinetic freeze-out temperature) of the emission source, but the effective temperature. As is well known, the interacting system at kinetic freeze-out (the last stage of collision) is influenced not only by thermal motion, but also by the flow effect. The real temperature of the emission source should reflect the thermal motion of the particles, and therefore the real temperature of the source is the kinetic freeze-out temperature. The effective temperature extracted from the elliptic flow spectrum includes thermal motion and the flow effect of the particles. By dissecting the effective temperature, it is possible to

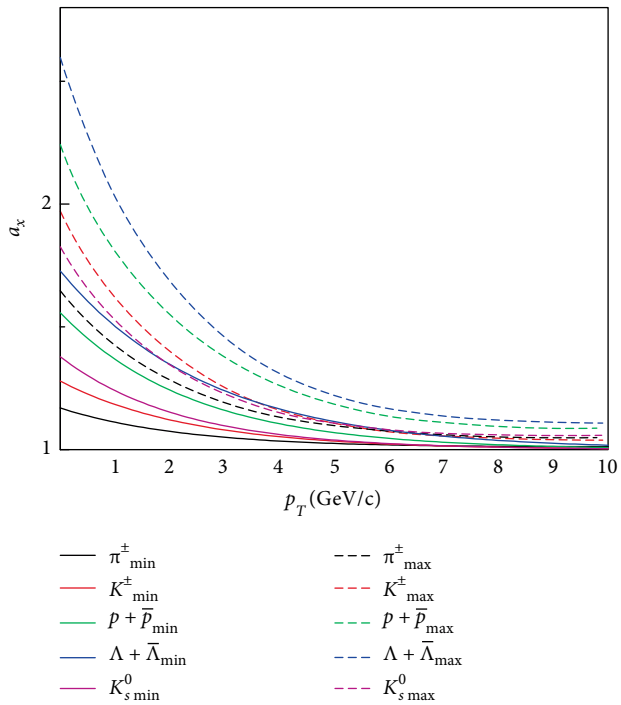

FIGURE 6: Transverse momentum dependency on the deformation parameter a_x of $\pi^{\pm}$, $K^{\pm}$, $p+\overline{p}$, $\Lambda+\overline{\Lambda}$, and K^0_s. The curves are the results of this fitted based on Equation (11).

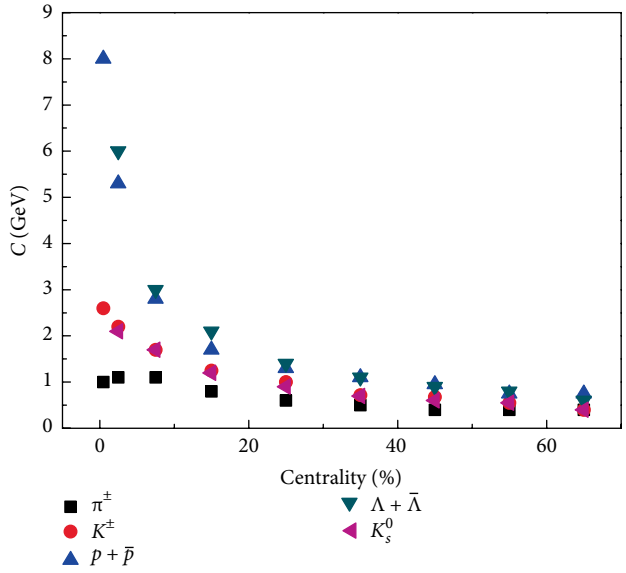

FIGURE 7: Free parameter C dependency on the centrality classes.

obtain the real temperature of the interacting system. The relationships between effective temperature, real temperature, and flow velocity are not totally clear. Therefore, the value of effective temperature obtained in this work is higher than the kinetic freeze-out temperature.

Table 1 shows that the parameter k_1 first increases rapidly with centrality percentage and then decreases slowly. It reaches a maximum as the centrality percentage reaches about 30%. In addition, Figure 6 shows that a_x decreases with increasing transverse momentum p_T. However, Figure 7 shows that the parameter C declines gradually from central to peripheral collisions. As for the dependency relationship, it can be readily understood.

From the participant-spectator geometric structure, it can be seen that as centrality percentage increases, the extent of the overlapping parts decreases, whereas the asymmetry rises. There is an approximate linear relationship between the elliptic flow and the eccentricity ratio of the participant. Hence, with increasing centrality percentage, the elliptic flow also grows. However, v_2 of particles in peripheral collisions is slightly smaller than in central collisions. This may be due to shorter system life under peripheral collisions, resulting in small v_2. Hence, k_1 first increases rapidly with the centrality percentage and then decreases slowly.

However, as the centrality percentage rises, the effective temperature C declines gradually. In accordance with the geometric structure of collisions, as the centrality percentage decreases, the number of involved nucleons increases, and the overlapping parts also increase, leading to higher energy density and strength of interaction, which manifests as higher temperature. The effective temperature C obtained in this study was higher than the true temperature. The reason for this was that the effective temperature incorporates the true temperature and the flow effect. The value excluding the flow effect should be equal to the true temperature. Figure 7 shows that for particles with considerable mass, the low variation ranges of effective temperature are similar.

In short, based on the multisource model, by introducing a Tsallis-Pareto-type function, the elliptic flow of identified particles generated in Pb–Pb collisions at $\sqrt{s_{NN}}$ = 5.02 TeV was correctly analyzed. Therefore, in the collision process, the asymmetry, expansion, and translation effects of geometric structure affect the dynamics of the final-state particles.

Data Availability

The data used to support the findings of this study are included within the article.

Ethical Approval

The authors declare that they are in compliance with ethical standards regarding the content of this paper.

Conflicts of Interest

The authors declare that they have no conflicts of interest regarding the publication of this paper.

Aknowledgments

This work was supported by the National Natural Science Foundation of China Grant Nos. 11447137 and 11575103 and the Doctoral Scientific Research Foundation of Taiyuan Normal University under Grant No. I170108.

References

[1] M. Aaboud et al. (ATLAS Collaboration), "Measurement of the $t^{-}tZ$ and $t^{-}t$ W cross sections in proton-proton collisions at $\sqrt{s}$=13 TeV with the ATLAS detector," *Physical Review D*, vol. 99, p. 072009, 2019.

[2] M. Aaboud et al. (ATLAS Collaboration), "Measurement of the four-lepton invariant mass spectrum in 13 TeV proton-proton collisions with the ATLAS detector," *Journal of High Energy Physics*, vol. 04, p. 048, 2019.

[3] M. Aaboud et al. (The ATLAS and CMS Collaborations), "Combinations of single-top-quark production cross-section measurements and $|f_{LV}V_{tb}|$ determinations at $\sqrt{s} = 7$ and 8 TeV with the ATLAS and CMS experiments," *Journal of High Energy Physics*, vol. 05, p. 088, 2019.

[4] R. Aaij et al. (LHCb Collaboration), "Measurement of B^{+}, B^{0} and Λ_b^0 production in pPb collisions at $\sqrt{s_{NN}} = 8.16$ TeV," *Physical Review D*, vol. 99, p. 052011, 2019.

[5] A. M. Sirunyan et al. (CMS Collaboration), "Measurement of the tt^{-} production cross section, the top quark mass, and the strong coupling constant using dilepton events in pp collisions at $\sqrt{s} = 13$ TeV," *European Physical Journal C*, vol. 79, p. 368, 2019.

[6] A. M. Sirunyan et al. (CMS Collaboration), "Observation of two excited B^{+}_{c} states and measurement of the B^{+}_{c} (2*S*) mass in *pp* collisions at $\sqrt{s} = 13$ TeV," *Physical Review Letters*, vol. 122, p. 132001, 2019.

[7] J. Adam et al. (STAR Collaboration), "Measurement of the longitudinal spin asymmetries for weak boson production in proton-proton collisions at $\sqrt{s} = 510$ GeV," *Physical Review D*, vol. 99, p. 051102, 2019.

[8] B. B. Back et al. (PHOBOS Collaboration), "The PHOBOS perspective on discoveries at RHIC," *Nuclear Physics A*, vol. 757, no. 1–2, pp. 28–101, 2005.

[9] C. Aidala et al. (PHENIX Collaboration), "Creation of quark–gluon plasma droplets with three distinct geometries ," *Nature Physics*, vol. 15, no. 3, p. 214, 2019.

[10] I. Arsene et al. (BRAHMS Collaboration), "Quark gluon plasma and color glass condensate at RHIC? the perspective from the BRAHMS experiment ," *Nuclear Physics A*, vol. 757, p. 1, 2005.

[11] K. Adcox et al. (PHENIX Collaboration), "Formation of dense partonic matter in relativistic nucleus-nucleus collisions at RHIC," *Nuclear Physics A*, vol. 757, p. 184, 2005.

[12] S. Chatrchyan et al. (CMS Collaborataion), "Measurement of the elliptic anisotropy of charged particles produced in PbPb collisions at $\sqrt{s}$NN = 2.76 TeV," *Physical Review C*, vol. 87, p. 014902, 2013.

[13] D. Derendarz et al. (ATLAS Collaboration), "Flow harmonics in Pb + Pb collisions at $\sqrt{S}$NN = 2.76 TeV with the ATLAS detector," *Nuclear Physics A*, vol. 931, p. 1002, 2014.

[14] B. Schenke, P. Tribedy, and R. Venugopalan, "Fluctuating glasma initial conditions and flow in heavy ion collisions," *Physical Review Letters*, vol. 108, p. 252301, 2012.

[15] V. Khachatryan et al. (CMS Collaboration), "Measurement of the transverse momentum spectrum of the Higgs boson produced in pp collisions at $\sqrt{s} = 8$ TeV using H→WW decays," *Journal of High Energy Physics*, vol. 03, p. 032, 2017.

[16] A. Adare et al. (PHENIX Collaboration), "Identified charged hadron production in p + pcollisions at $\sqrt{s} = 200$ and 62.4 GeV," *Physical Review C*, vol. 83, p. 064903, 2011.

[17] B. Abelev et al. (ALICE Collaboration), "Pseudorapidity Density of Charged Particles in p + PbCollisions at $\sqrt{s_{NN}} = 5.02$ TeV," *Physical Review Letters*, vol. 110, p. 032301, 2013.

[18] G. J. Alner et al. (UA5 Collaboration), "A general study of proton-antiproton physics at $\sqrt{s} = 546$-GeV," *Physics Reports-Review Section of Physics Letters*, vol. 154, p. 247, 1987.

[19] Z. Valentina et al. (ALICE Collaboration), "Charged-particle multiplicity distributions over a wide pseudorapidity range in proton–proton collisions with ALICE," *Nuclear Physics A*, vol. 956, pp. 529–532, 2016.

[20] A. Adare et al. (PHENIX Collaboration), "Measurement of higher cumulants of net-charge multiplicity distributions in Au + Au collisions at $\sqrt{s_{NN}} = 7.7 - 200$ GeV," *Physical Review C*, vol. 93, p. 011901, 2016.

[21] S. Acharya et al. (ALICE Collaboration), "Anisotropic flow in Xe–Xe collisions at $\sqrt{s_{NN}} = 5.44$ TeV," *Physics Letters B*, vol. 784, p. 82, 2018.

[22] M. Aaboud et al. (ATLAS Collaboration), "Measurement of the azimuthal anisotropy of charged particles produced in $\sqrt{s_{NN}} = 5.02$ TeV Pb + Pb collisions with the ATLAS detector," *European Physical Journal C*, vol. 78, p. 997, 2018.

[23] D. Solanki, P. Sorensen, S. Basu, R. Raniwala, and T. K. Nayak, "Beam energy dependence of elliptic and triangular flow with the AMPT model," *Physics Letters B*, vol. 720, no. 4–5, pp. 352–357, 2013.

[24] G. Aad et al. (ATLAS Collaboration), "Measurement of the pseudorapidity and transverse momentum dependence of the elliptic flow of charged particles in lead–lead collisions at $\sqrt{s_{NN}} = 2.76$ TeV with the ATLAS detector," *Physics Letters B*, vol. 707, pp. 330–348, 2012.

[25] K. Aamodt et al. (ALICE Collaboration), "Elliptic Flow of Charged Particles in Pb–Pb Collisions at $\sqrt{s_{NN}} = 2.76$ TeV," *Physical Review Letters*, vol. 105, p. 252302, 2010.

[26] B. I. Abelev et al. (STAR Collaboration), "Charged and strange hadron elliptic flow in Cu + Cucollisions at $\sqrt{s_{NN}} = 62.4$ and 200 GeV," *Physical Review C*, vol. 81, p. 044902, 2010.

[27] S. Afanasiev et al. (PHENIX Collaboration), "Elliptic flow for phi mesons and (anti)deuterons in Au+Au collisions at sqrt(s_ NN) = 200 GeV," *Physical Review Letter*, vol. 99, p. 052301, 2007.

[28] C. Alt et al. (NA49 Collaboration), "Directed and elliptic flow of charged pions and protons in Pb + Pbcollisions at 40 A and 158 AGeV," *Physical Review C*, vol. 68, p. 034903, 2003.

[29] A. M. Poskanzer et al. (NA49 Collaboration), "Centrality dependence of directed and elliptic flow at the SPS," *Nuclear Physics A*, vol. 661, pp. 341–344, 1999.

[30] L. Adamczyk et al. (STAR Collaboration), "Centrality and transverse momentum dependence of elliptic flow of multistrange hadrons and ϕ meson in Au+Au collisions at $\sqrt{s_{NN}} = 200$ GeV," *Physical Review Letters*, vol. 116, p. 062301, 2016.

[31] S. Voloshin and Y. Zhang, "Flow study in relativistic nuclear collisions by fourier expansion of azimuthal particle distributions," *Journal of Physics C*, vol. 70, no. 4, pp. 665–671, 1996.

[32] A. M. Poskanzer and S. A. Voloshin, "Methods for analyzing anisotropic flow in relativistic nuclear collisions," *Physical Review C*, vol. 58, p. 1671, 1998.

[33] Y.-H. Chen and F.-H. Liu, "Event patterns extracted from anisotropic spectra of charged particles produced in Pb–Pb

collisions at 2.76 TeV," *European Physical Journal A*, vol. 53, p. 230, 2017.

[34] E. Q. Wang, H. R. Wei, B. C. Li, and F. H. Liu, "Dependence of elliptic flow on participant nucleon number in Au + Au collisions at $\sqrt{s_{NN}} = 200$ GeV," *Physical Review C*, vol. 83, p. 034906, 2011.

[35] B.-C. Li, Y.-Y. Fu, E.-Q. Wang, X.-J. Wen, and F.-H. Liu, "Dependence of elliptic flow on transverse momentum in $\sqrt{s_{NN}} = 200$ GeV Au-Au and $\sqrt{s_{NN}} = 2.76$ TeV Pb–Pb collisions," *Chinese Physics Letters*, vol. 29, no. 7, p. 072501, 2012.

[36] S. Acharya et al. (ALICE Collaboration), "Anisotropic flow of identified particles in Pb–Pb collisions at $\sqrt{s_{NN}} = 5.02$ TeV," *Journal of High Energy Physics*, vol. 09, p. 006, 2018.

[37] K. Werner, "Strings, pomerons and the VENUS model of hadronic interactions at ultrarelativistic energies," *Physics Reports-Review Section of Physics Letters*, vol. 232, p. 87, 1993.

[38] G. D. Westfall, J. Gosset, P. J. Johansen et al., "Nuclear fireball model for proton inclusive spectra from relativistic heavy-ion collisions," *Physical Review Letters*, vol. 37, p. 1202, 1976.

[39] F. H. Liu and Y. A. Panebratsev, "Pseudorapidity distribution of shower particles in heavy ion induced interactions in nuclear emulsion at high energy," *Physical Review C*, vol. 59, p. 1798, 1999.

[40] F. H. Liu and Y. A. Panebratsev, "Baryon rapidity distribution in nucleus-nucleus collisions at ultrarelativistic energies," *Physical Review C*, vol. 59, p. 1193, 1999.

[41] F. H. Liu and J. S. Li, "Isotopic production cross section of fragments in ^{56}Fe+p and ^{136}Xe(^{124}Xe) + Pb reactions over an energy range from 300 A to 1500 AMeV," *Physical Review C*, vol. 78, p. 044602, 2008.

[42] F. H. Liu, "Unified description of multiplicity distributions of final-state particles produced in collisions at high energies," *Nuclear Physics A*, vol. 810, no. 1–4, pp. 159–172, 2008.

[43] F. H. Liu, N. N. Abd Allah, and B. K. Singh, "Dependence of black fragment azimuthal and projected angular distributions on polar angle in silicon-emulsion collisions at 4.5 AGeV/c," *Physical Review C*, vol. 69, p. 057601, 2004.

[44] F. H. Liu, "Longitudinal and transverse flows of protons in 2–8 AGeV Au − Au collisions," *Europhysics Letters*, vol. 63, no. 2, p. 193, 2003.

[45] F. H. Liu, Y. Q. Gao, T. Tian, and B. C. Li, "Unified description of transverse momentum spectrums contributed by soft and hard processes in high-energy nuclear collisions," *European Physical Journal A*, vol. 50, p. 94, 2014.

[46] A. M. Sirunyan et al. (CMS Collaboration), "Measurement of charged pion, kaon, and proton production in proton-proton collisions at $\sqrt{s} = 13$ TeV," *Physical Review D*, vol. 96, p. 112003, 2017.

[47] C. Tsallis, "Possible generalization of Boltzmann-Gibbs statistics," *Journal of Statistical Physics*, vol. 52, no. 1–2, pp. 479–487, 1988.

[48] T. S. Biro, G. Purcsel, and K. Urmossy, "Non-extensive approach to quark matter," *The European Physical Journal A*, vol. 40, pp. 325–340, 2009.

[49] V. Khachatryan et al. (CMS Collaboration), "Transverse-momentum and pseudorapidity distributions of charged hadrons in pp collisions at $\sqrt{s} = 0.9$ and 2.36 TeV," *Journal of High Energy Physics*, vol. 02, p. 041, 2010.

[50] X. W. He, H. R. Wei, and F. H. Liu, "Chemical potentials of light hadrons and quarks from yield ratios of negative to positive particles in high energy pp collisions," *Journal of Physics G: Nuclear and Particle Physics*, vol. 46, p. 025102, 2019.